A General Equation for Stress Concentration in Countersunk Holes

Kunigal N. Shivakumar[1], Anil Bhargava[2] and Sameer Hamoush[3]

Abstract: A detailed and accurate three-dimensional finite element stress analysis was conducted on countersunk rivet holes in a plate subjected to tension loading. The analysis included a wide range of countersunk depths, plate thicknesses, countersunk angles and plate widths. The study confirmed some of the previous results, addressed their differences, provided many new results, and investigated countersunk angle and width effects. Using the detailed FE results and the limiting conditions, a general equation for stress concentration was developed and verified.

Keyword: Stress concentration factor, countersink, countersunk holes, tensile loading, stress concentration equation, finite element analysis

Nomenclature

b	straight-shank depth
C_s	countersink depth $(t - b)$
E	Young's modulus
FEA	finite element analysis
h	one-half height of plate
K_t	maximum stress-concentration factor along bore of hole under tension
r	radius of straight-shank portion of hole
SCF	stress concentration factor
SS	straight-shank
t	plate thickness
w	plate half-width
x, y, z	Cartesian coordinate system

[1] Corresponding author. Tel.: 336-334-7411 x 2112; fax: 336-256-0873. E-mail address: kunigal@ncat.edu. Department of Mechanical and Chemical Engineering, Center for Composite Materials Research, North Carolina A & T State University, Greensboro, NC 27411.

[2] Infosys Technologies Limited, 6100 Tennyson Parkway Suite 200, Plano, TX 75024.

[3] Department of Civil and Architectural Engineering, Center for Composite Materials Research, North Carolina A & T State University, Greensboro, NC 27411.

ν	Poisson's ratio
θ_c	countersink angle
σ_0	applied remote tension stress

1 Introduction

Riveting is a common method of joining structural components. Joining introduces discontinuities (stress risers) in the form of holes, change in load path, and additional secondary loads such as rivet bearing and bending. Because of these reasons, local stresses at the joint are elevated compared to structural nominal stresses. Wherever the aero/hydro dynamic surfaces are required, countersunk rivets are often used. Countersinking further complicates the stress flow and causes additional elevation of local stresses. These problems require a three dimensional (3-D) analysis. Accurate determination of local stresses is essential to predict joint strength and fatigue life of the component.

Exhaustive studies on stress concentration in holes and notches for two-dimensional (2-D) bodies subjected to a wide variety of loadings have been reported in the literature and in handbooks [Pilkey (1997), Savin (1961)]. Three-dimensional (3-D) results have been reported for plates with circular (straight-shank) holes subjected to remote tension [Green (1948), Neuber (1946), Sternberg and Sadowsky (1949), Folias and Wang (1990), Shivakumar and Newman (1992, 1995), Whaley (1965)]. All these solutions were limited to wide plates. A summary of these are listed below.

1. Stress concentration is due to hoop stress along the bore of the hole.

2. Stress concentration factor (SCF) depends on the dimensionless parameters (t/r) and (z/t), where z is the thickness co-ordinate direction and t is the plate thickness.

3. Stress concentration is highest in the mid-thickness of the plate for thin to moderately thick plates, but for thick plates, the stress concentration peaks near the free surface, (at about $t/10$)

4. The state-of-stress is nearly plane-strain in the central region, is nearly plane-stress at the free surface and is intermediate in the transition region. Thus, the stress flows into the central region of the plate causing higher stress concentration than at the plate surface.

5. The stress concentration is about 4 to 7% higher than plane-stress value ($K_t = 3$) and it increases with plate thickness. Plane-stress value is recovered for very thin plates. The stress concentration is about 10% lower than plane-stress value at the free surface.

Only few papers have been published for countersunk rivet holes that directly relate to stress concentration. The first was by Whaley (1965), using birefringent coating on aluminum plates. He measured the stresses on the surface of the plate instead of measuring in the interior of the hole. The other experimental work was by Cheng (1978); he used stress freezing technique to obtain stress through the thickness of plate with a countersunk hole. He investigated a total of 13 configurations with different countersink angles and depths; seven specimens for tension loading and six for bending loading. Cheng's results showed conclusively that the highest stress concentration is at the edge of the countersink. In early 1990, Shivakumar and Newman (1992, 1995) conducted a detailed 3-D FE analysis of countersunk holes in a wide plate subjected to tension, bending and wedge loadings. Their study included a wide range of countersink depth to thickness ratio (C_s/t), plate thickness to radius ratio (t/r), and a countersunk angle (θ_c) of 100°. Numerical results were presented in the form of charts, tables along with a simple FORTRAN program including an interpolation method to determine K_t for a wide plate and countersunk angle of 100°. In 1993, Young and Lee (1993) conducted an independent 3-D FE analysis of plates with countersunk holes subjected to tension load and

proposed a design equation by combining their FE results and British Aerospace's 2-D design equation. Young and Lee's solutions were based on a very coarse FE model and their equation even did not reduce to 2-D solution in literature. Furthermore, Shivakumar and Newman's and Young and Lee's solutions differed widely for $C_s/t = 1$. Therefore, the present study is undertaken to verify the two results, provide new results, and then to develop an accurate stress concentration factor equation that satisfies the limiting conditions of the configurations. An exhaustive 3-D FE study with very fine modeling will be conducted by different countersunk angle (θ_c), thickness to radius (t/r) ratio, countersink depth to thickness (C_s/t) ratio and plate width to radius (w/r) ratio. Based on these results and limiting configurational conditions, an equation for SCF in countersunk hole will be developed. Results and equations obtained from the preliminary studies conducted by the authors have already been presented in Shivakumar, Bhargava and Hamoush (2006). This paper presents an improved equation compared to the previous equation.

Meshless methods have been developed in references Li1, Shen, Han, and Atluri (2003), and Chen and Chen (2005), to solve problems in three-dimensional elasticity with singularities and material discontinuities.

2   Configuration and Material

Figure 1 shows a configuration of a plate with a countersunk rivet hole subjected to tension. All the geometric parameters used in this study are defined in the figure. The Cartesian coordinates $x - y - z$ represent the reference coordinate system. The plate width and the height are, respectively, $2w$ and $2h$, and the thickness is t. The plate is subjected to a remote tensile stress, σ_0. The countersunk hole consists of a straight-shank part (thickness b) and a countersunk part (thickness C_s). The total depth t of the hole, which is also the thickness of the plate, is related to b and C_s by $t = b + C_s$. The radius of the SS part of the hole is r and the countersunk angle is θ_c. A common angle of countersink used in aircraft construction is 100°; the K_t results evaluated for this angle are
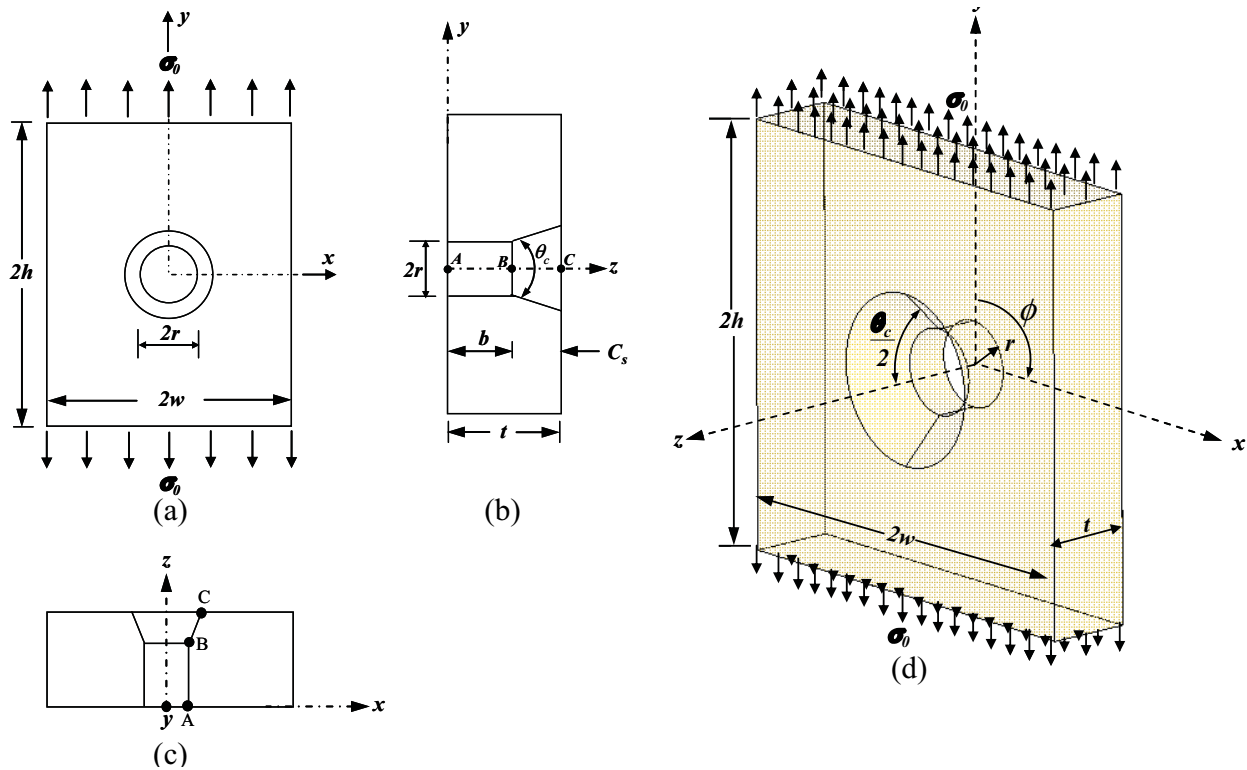
Figure 1: Configuration and Nomenclature of a Countersunk Rivet Hole: (a) $x - y$ Plane; (b) $y - z$ Plane; (c) $z - x$ Plane; (d) 3-D Configuration

considered to be the baseline. The variation of parameters C_s, t and θ_c will simulate all cases of hole configurations from SS ($C_s/t = 0$) to knife-edge ($C_s/t = 1$).

The material is assumed to be homogeneous and isotropic with E = 68.9 GPa and ν = 0.3. Any value of E is acceptable, because in an isotropic problem subjected to force boundary conditions the resulting stresses are independent of E. Thus the SCF is independent of E. However, the Poisson's ratio ν may influence the results but its effect is secondary and neglected.

3 Definition of Stress-Concentration Factor

The 2-D stress concentration factor definition is given in many classical books on theory of elasticity and in stress concentration handbooks. For 3-D configurations, the stress concentration varies along the bore of the hole. Therefore, the stress concentration becomes a function of z coordinate along the line formed by the intersection of $y = 0$ plane and the hole. The line connecting the points

A, B, C in Figure 1 (b) and (c) defines the path of interest. The stress concentration $K_t(z)$ is the ratio of hoop stress σ_{yy} along the line A-B-C and the remote stress σ_0, $K_t(z) = \sigma_y(z)/\sigma_0$. The stress concentration factor K_t is the maximum of $K_t(z)$.

4 Finite-Element Analysis

A commercial FE analysis code, ANSYS Version 10, was used for geometric modeling, FE modeling and analysis of the problem. ANSYS Parametric Design Language (APDL) programs were written to automatically generate geometric and FE models, imposition of loading and boundary conditions, and conducting the analysis in a batch mode.

4.1 Geometric Models

The various geometric parameters considered in the study have been presented in the previous section 2. Because the geometry and the loading are symmetric (Fig. 1), only the symmetric-quarter of the model was considered. Figure 2 illustrates

(a)

(b)

(c)
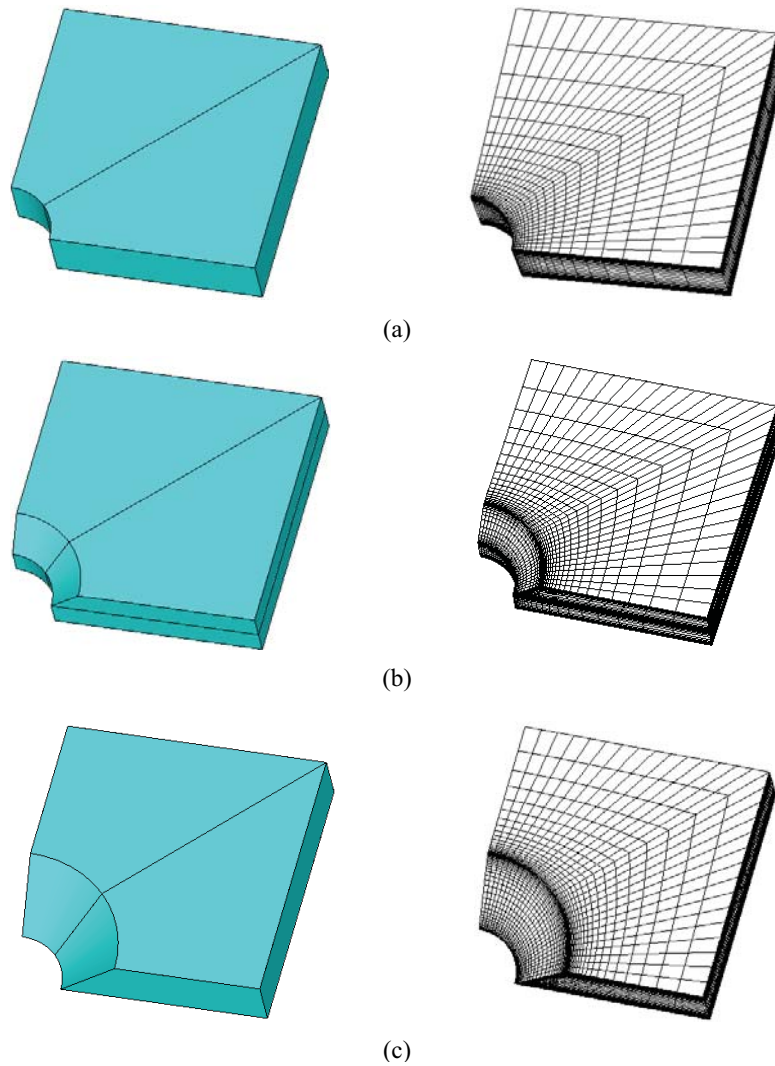
Figure 2: Quarter Symmetric Geometric and FE Models Showing the Effect of C_s/t: (a) Straight-Shank Hole ($w/r = h/r = 5$, $C_s/t = 0$, $t/r =1$); (b) Countersunk Hole ($w/r = h/r = 5$, $C_s/t = 0.5$, $t/r = 1$); (c) Knife- Edge Hole ($w/r = h/r = 5$, $C_s/t = 1$, $t/r = 1$)
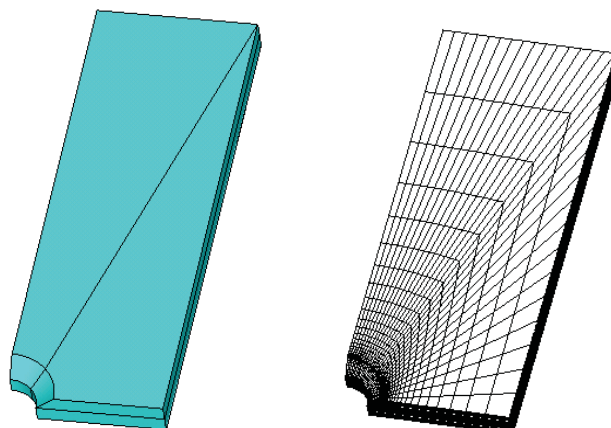
Figure 3: Quarter Symmetric Geometric and FE Models of Narrow Width ($w/r = 6$, $h/r = 15$, $C_s/t = 0.5$, $t/r = 1$)

the three possible countersink rivet hole configurations, namely, SS ($(C_s/t) = 0$), typical countersink, and knife-edge ($(C_s/t) = 1$). Figure 3 shows a narrow width model used for conducting a study on width effect.

4.2 FE Models

Three-dimensional hexahedron elements (solid45) were generated over the volumes using the iso-parametric mapping concept. Care was taken in generating the elements so that only hexahedron elements were generated. The FE mesh idealization was finer in the high stress gradient regions and coarser at the low or no stress gradient regions. Three levels of mesh refinements were used to conduct the convergence study. Results of the convergence study will be presented later. The Figs. 2 and 3 illustrate the typical FE meshes used for SS, countersunk and knife-edge geometries, and narrow width plates.

4.3 Boundary Conditions, Loading and Analysis

Symmetry boundary conditions were imposed on the model by constraining u_y displacement in y-direction on $y = 0$ plane and the u_x displacement in x-direction on $x = 0$ plane. To arrest the rigid body motion in z-direction, the u_z displacement was restrained at a node at $x = z = 0$ and $y = r$. The plane $y = h$ was loaded with a uniform stress $\sigma_0 = 1$. All other boundary regions were allowed to deform freely. A linear FE stress analysis was conducted. Deformation, stress and strain field were examined. The hoop stresses along the nodal line A-B-C, (see Fig. 1 (c)) were extracted from the APDL program. These stresses directly gave the stress concentration, $K_t(z)$ and the maximum value of $K_t(z)$ is the stress concentration factor K_t.

4.4 Mesh Convergence Study

A mesh convergence study was conducted to evaluate the accuracy of the K_t results. The geometric model employed for this study was $t/r = 1$, $w/r = 3$ and $(C_s/t) = 0.75$. The three specific meshes were studied: baseline, finer and finest. To provide a clear picture of the refinement, the mesh regions around the countersunk hole are enlarged

and shown in Fig. 4. The finer mesh was obtained by doubling the number of divisions in all three directions. The finest mesh was also obtained by doubling the divisions but only in the area of interest. The mesh convergence approach used was similar to the patch test defined in Zienkiewicz and Taylor (1989). Figure 5 shows K_t for the three meshes and note that the finest mesh result has almost reached the asymptotic value. The baseline and the finer mesh K_t differed by 1.4 and 0.2 percent, respectively compared to the finest mesh. These errors are small and are assumed to be acceptable. Therefore, the baseline mesh was used in all other studies. Details of this study are given by Bhargava (2006).

5 Comparison of Present FE Results with Literature

The K_t results from the present finite element models are compared with other finite element and experimental results in the literature.

5.1 Comparison with Other FE Results

The present baseline FE model results were compared with Shivakumar and Newman's (1992 and 1995) revised FE results (which had some minor mistakes) for different thickness-to-hole radius ratios (t/r) of 0.5, 1, 2 and 4 with $w/r = 15$ and $\theta_c = 100°$. The present FEA results and Shivakumar and Newman's results agreed very well for all cases, the difference was less than 1%.

Young and Lee's FE results are compared with the present FE results by plotting the variation of K_t as a function of (C_s/t) for different plate widths of $w/r = 3$, 4, 5 and 6, in Fig. 6. The present FE are represented by solid symbols and joined by solid lines while Young and Lee's FE results are represented by hollow symbols. From Fig. 6 it is clear that for all values of $C_s/t > 0.5$, Young and Lee's results are consistently higher than the present FE results. The difference is largest and is about 32% for $C_s/t = 1$ with $w/r = 3$. The reason for this difference is be due to coarseness of the FE mesh used in Young and Lee's study.

(a)   (b)   (c)
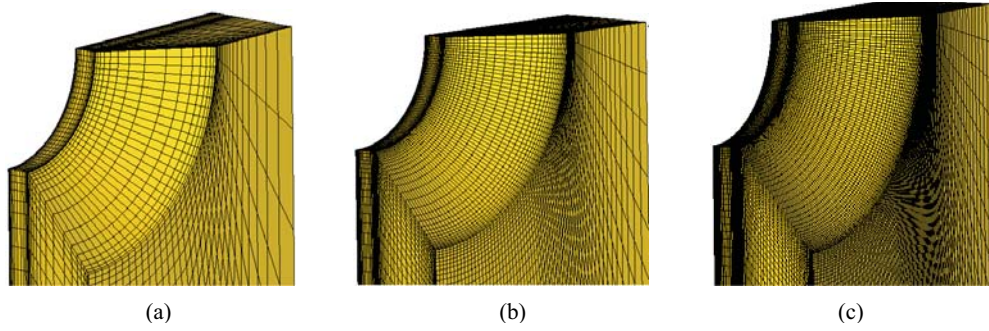
Figure 4: Mesh Sizes Used for the Convergence Study: (a) Baseline; (b) Finer; (c) Finest
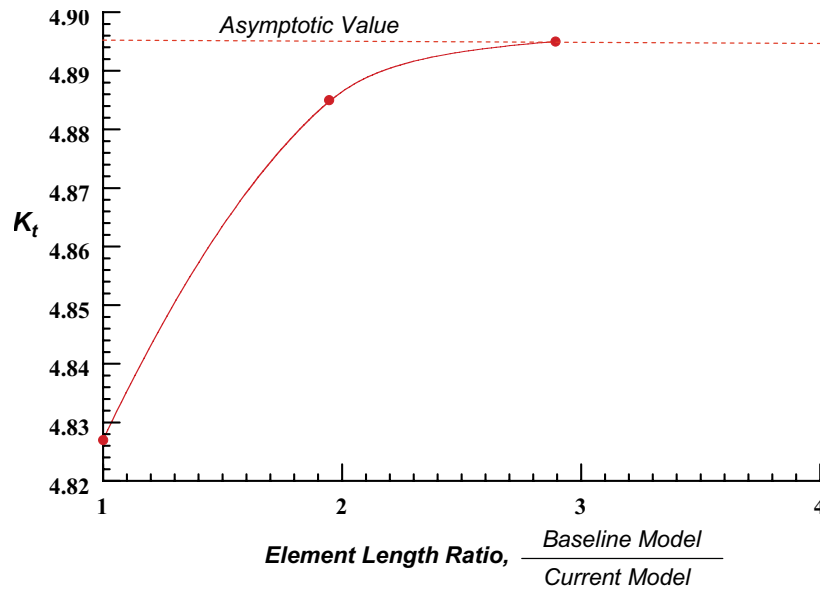
Figure 5: Plot of K_t for the Three Mesh Refinements
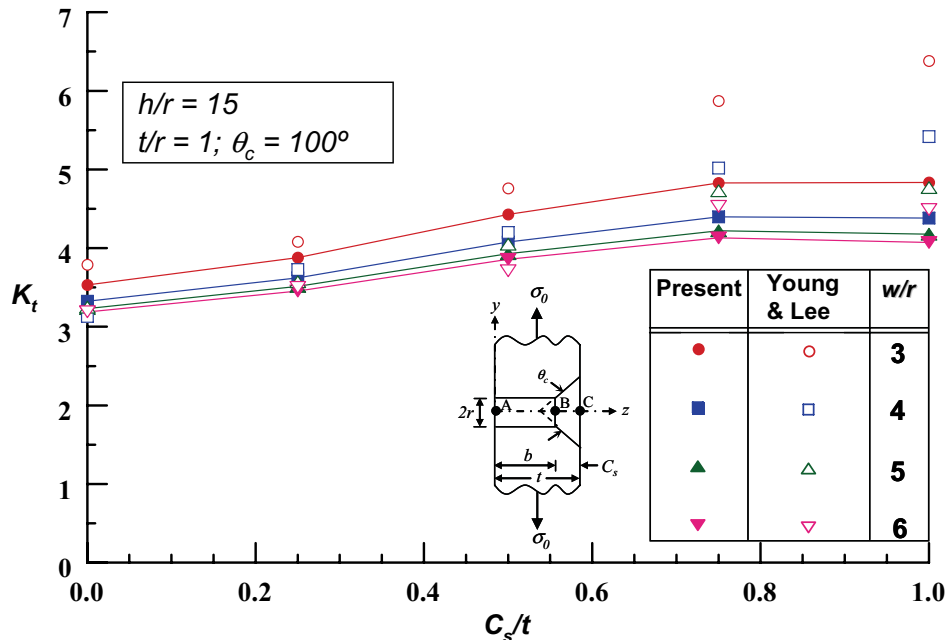
Figure 6: Comparison of Present and Young and Lee's FE K_t Results

Table 1: Comparison of K_t from Cheng's Experimental Results with Current FEA

Model #	θ_c Degrees	C_s/t	w/r	h/r	t/r	K_t		Percent Difference
						Cheng's Expt.	Present FEA	
1	60	0.40	7.14	22.01	4.15	3.44	3.79	-9.2
2	80	0.40	7.14	22.01	4.78	3.50	4.07	-14.0
3	82	0.40	10.00	30.70	5.79	3.48	4.10	-15.1
4	82	0.40	7.14	22.01	4.15	3.54	4.02	-11.9
5	82	0.40	5.00	15.28	2.88	3.13	4.02	-22.1
6	82	0.55	7.14	22.01	4.15	3.43	4.34	-21.0
7	90	0.40	7.14	22.01	4.15	3.41	4.11	-17.1

5.2 Comparison with Experiments

Finite element models for all of Cheng's experimental models were generated and the stress concentration factor was determined. Cheng's experimental configurations, his results, and the present FEA results are listed in Table 1. The percent differences for all seven models are also summarized. The percent difference is defined as $(K_{teq.} - K_{tFEA})/K_{tFEA} \times 100$. Cheng's experimental results were 9% to 22% lower than the FE results. These differences are due to experimental inaccuracies which are because of the number of variables involved in the stress-freezing technique, for example the cutting of the specimens into slices, the subsequent measurements of the isochromatic fringes and the difficulty in measuring the stresses at the countersunk edge.

Shivakumar and Newman (1992, 1995) and Young and Lee (1993) have also compared their FE results with Cheng's (1978) experimental data. For model #7, Shivakumar and Newman's result was 5% higher, and Young and Lee's result was 7% lower than the present FE results.

6 Stress Concentration Results from FE Analysis

As previously mentioned, a detailed three-dimensional finite element analysis was conducted for a wide range of (C_s/t), t/r, θ_c and w/r parameters to evaluate their effect on SCF. Throughout the analysis, $h/r = 15$ was used so that the loading ($\sigma_0 = 1$) could be considered remote with no or very little influence on the hole geometry. The values of (C_s/t) were 0 (straight-shank hole), 0.25, 0.5, 0.75 and 1.0 (knife-edge) and the t/r values were 0.5, 1, 2 and 4. The plate width-to-hole radius ratio, w/r, was varied from 2.5 to 15 and the countersunk angle θ_c was varied from 60º to 130º. The influence of θ_c on the SCF was first assessed by performing the analysis for θ_c values ranging from 0º through 170º in increments of 10º for $C_s/t = 0.25$ and $t/r = 1.0$. Additional analyses were also conducted to evaluate the effect of θ_c in combination with the countersunk depth ratio (C_s/t) and the plate thickness ratio (t/r) on K_t. Secondly, the effect of C_s/t and t/r were assessed for a wide plate ($w/r = 15$) with $\theta_c = 100º$ by performing analyses by varying C_s/t and t/r. Finally, the effect of the plate width-to-hole radius ratio w/r was assessed for a countersink configuration with $\theta_c = 100º$ by performing an analysis for $w/r = 2.5$ to 15. The results of the analyses are presented in the following sub-sections. Although the SS hole configuration is different from that of the countersunk hole, for the purpose of presentation and discussion it is considered to be a special case of the countersunk hole with $C_s/t = 0$. The stress concentration $K_t(z)$ along the bore of the hole (ABC of Fig. 1) was examined. The maximum value of $K_t(z)$, that is K_t, was extracted for further analysis.

6.1 Effect of countersunk angle (θ_c)

Figure 7 shows the variation of $K_t(z)$ along z/t for θ_c values ranging from 60º to 120º (including the results for $\theta_c = 100º$) for $h/r = w/r = 15$, $t/r = 1$ and $C_s/t = 0.25$. The $K_t(z)$ is maximum at the countersink (B) and it decreases towards both the free edges. The $K_t(z)$ decreases much more
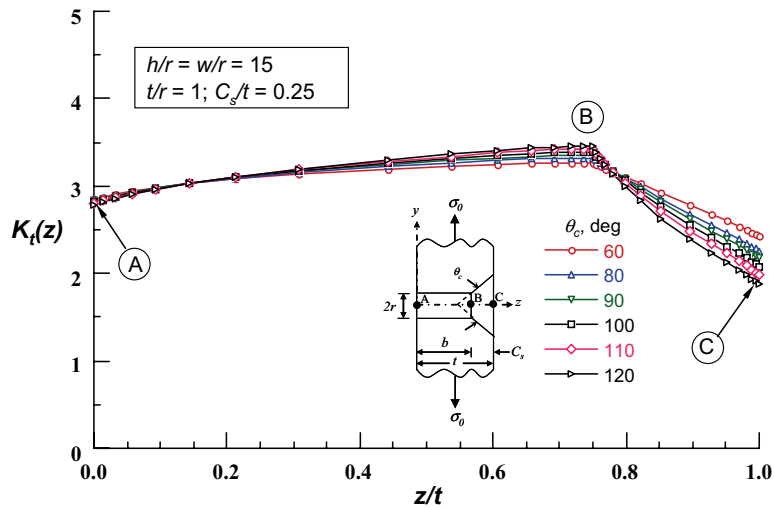
Figure 7: Effect of countersink angle θ_c on $K_t(z)$ for a wide plate
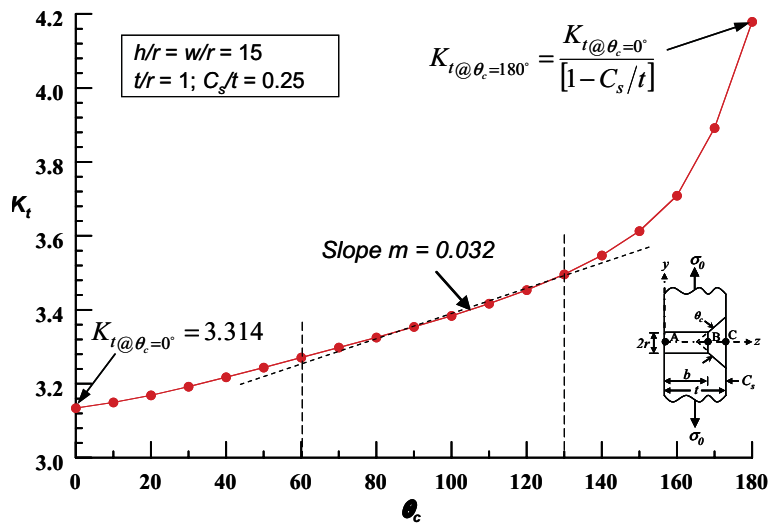
Figure 8: Variation of K_t with θ_c ($w/r = h/r = 15$; $(C_s/t) = 0.25$; $t/r = 1$)
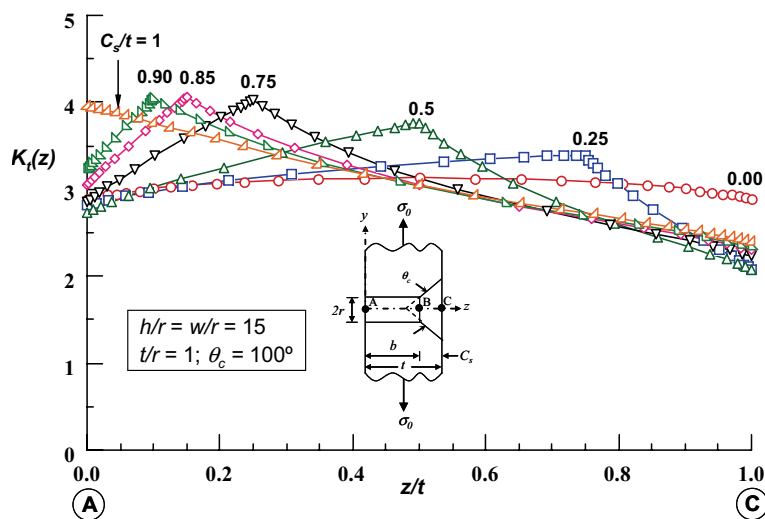
Figure 9: Effect of Countersunk Depth on Stress Concentration Distribution for a Wide Plate ($t/r = 1$)

rapidly towards the countersunk part (B-C) than towards the straight shank part (B-A). The $K_t(z)$ at C is lower than that at A. The $K_t(z)$ at B increases with θ_c. This trend is in agreement with Shivakumar and Newman's (1992, 1995) results while Young and Lee's (1993) results showed an opposite trend. The difference in K_t between $\theta_c = 90^o$ and 100° and between $\theta_c = 100^o$ and 110° is about 1%; therefore, for a small deviation ($\pm 10^o$) of θ_c from 100°, K_t can be assumed constant. Figure 8 presents the K_t for a larger range (0° to 180°) of θ_c, for $(C_s/t) = 0.25$ and $t/r = 1$. The K_t for $\theta_c = 0$ is from the SS hole for $t/r = 1$ and the K_t value for θ_c of 180° is extrapolated from the following equation for the loss of plate thickness equal to C_s/t.

$$K_{t@\theta_c=180^o} = \frac{K_{t@\theta_c=0^o}}{[1 - C_s/t]} \tag{1}$$

The K_t has a nonlinear relation with θ_c; however, for a range of $60^o \leq \theta_c \leq 130^o$, θ_c effect can be approximated by a linear relation as illustrated by the broken line in Fig. 8. The reason for the monotonic increase in K_t with θ_c, is because of continuous channeling of load towards the countersink edge and around the hole as θ_c increases [Bhargava (2006)].

6.2 Effect of countersink depth (C_s/t)

The distribution of $K_t(z)$ along z/t for varying countersink depths is shown in Figure 9 to 13 for $t/r = 1$. For thin plates ($t/r \leq 1$), the maximum of $K_t(z)$, that is K_t, occurs at the countersink edge. For thicker plates ($t/r = 2$ and 4) and $C_s/t \leq 0.25$, K_t occurs not at the countersink edge but slightly away from the edge (5% of t) and towards the SS portion of the hole. This trend continues for all shallow countersink configurations. The K_t values generated for different values of C_s/t and t/r are listed in Table 2 and plotted in Fig. 10. These results show that K_t increases monotonically with C_s/t until C_s/t is equal to about 0.8 and then decreases for all plate thicknesses less than $2r$. For thick plates, $t \geq 2r$, K_t continues to increase with C_s/t (including the knife-edge case), as also noted by Shivakumar and Newman (1992, 1995). Figure 10 also shows that K_t increases monotonically with t/r.

6.3 Effect of thickness to radius ratio (t/r)

Figures 11 illustrates the effect of t/r on $K_t(z)$ for $(C_s/t) = 0.5$. Values of $t/r = 0.5$, 1 and 2 represent the practical range of hole configurations used in the aircraft industry and $t/r \geq 2$ is used for thick structures such as those found in marine applications. The $K_t(z)$ increases monotonically with t/r on the SS portion of the hole except near the free edge, while it decreases with t/r on the countersunk portion of the hole. But the K_t increases with t/r as illustrated in Figs. 11 and 12. As also noted in the previous section, K_t increases with plate thickness (t/r) and countersunk depth (C_s/t). The variation of K_t is nonlinear and coupled with both C_s/t and t/r.

6.4 Effect of width to radius ratio (w/r)

The rate of change of $K_t(z)$ and K_t with w/r is higher for smaller w/r and is small for larger w/r. More details for different C_s/t are in Bhargava (2006). The K_t plot is shown in Fig. 14. Here also, K_t increases rapidly for $w/r < 3$ and becomes infinity for $w/r = 1$, as predicted. For $w/r > 6$, K_t is nearly constant indicating that for wide plates K_t is independent of w/r. The plot also includes Heywood's (1952) 2-D solution; the differences between the two are due to the 3-D effect, which is not much. Such a close agreement indicates that Heywood's width correction equation could be used for countersunk hole K_t.

The K_t versus w/r for different (C_s/t) values with $t/r = 1$ and $\theta_c = 100^o$ are shown in Fig. 15 and the values of K_t are listed in Table 3. As shown in the figure, the K_t increases rapidly as w/r becomes smaller and it becomes almost constant for $w/r > 6$.

7   3-D Equation for Stress Concentration Factor (K_t)

Results of FE results can be summarized as follows:

1. The K_t occurs at or near the countersink.

   (a) K_t is a function of t/r for SS holes.
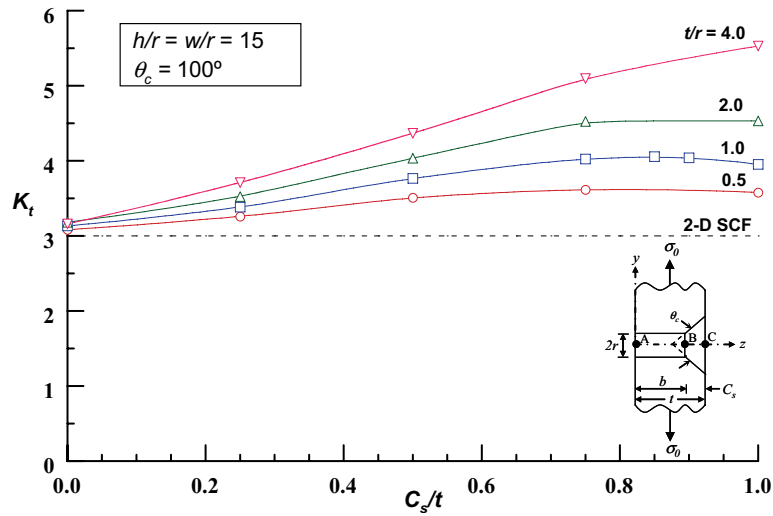
Figure 10: Variation of Maximum SCF as a Function of (C_s/t)
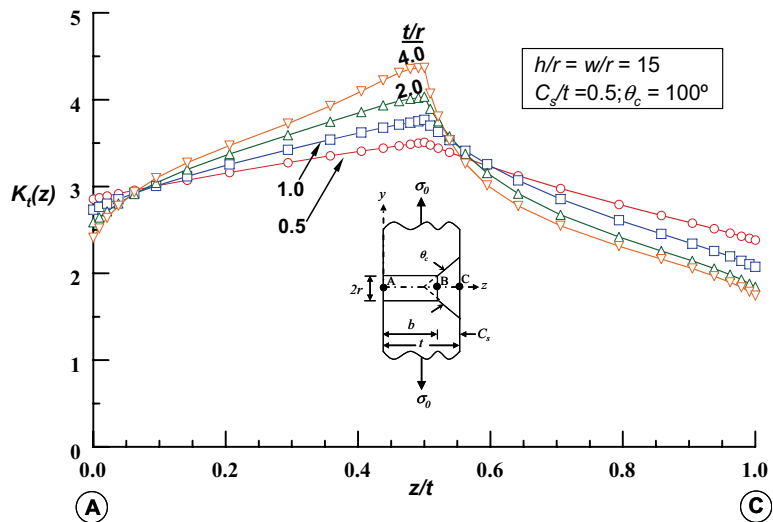
Figure 11: Effect of t/r on Stress Concentration Distribution for $C_s/t = 0.5$
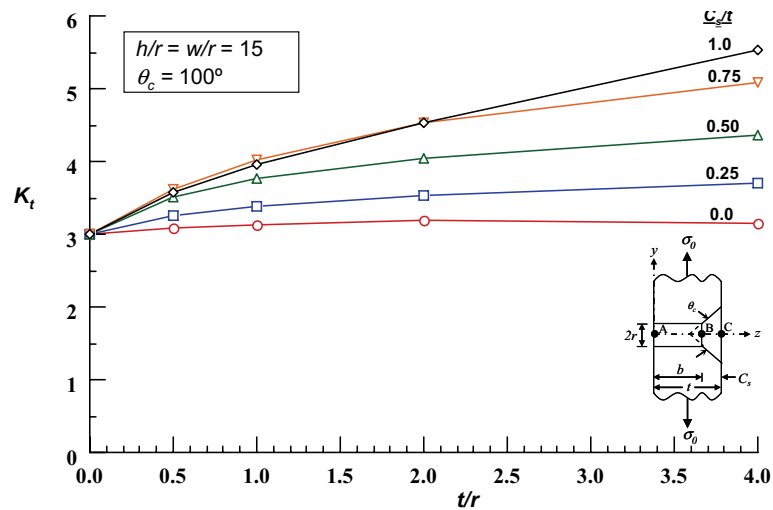
Figure 12: Variation of Maximum SCF as a Function of t/r
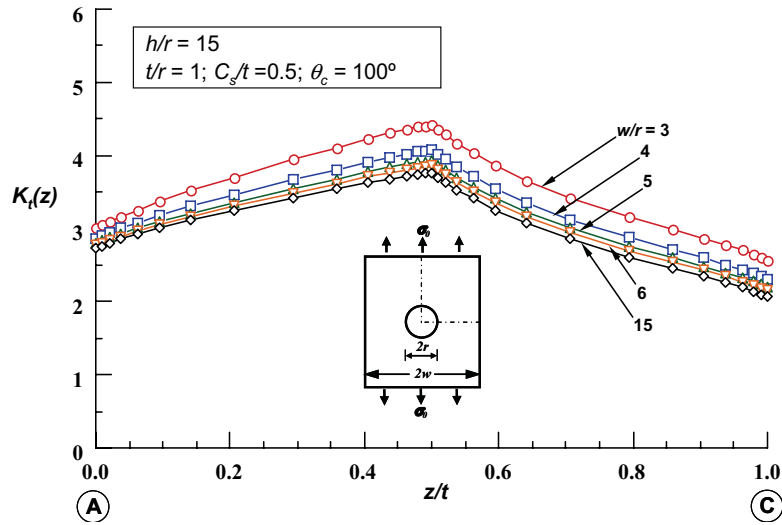
Figure 13: Effect of w/r on Stress Concentration Distribution ($C_s/t = 0.5$)
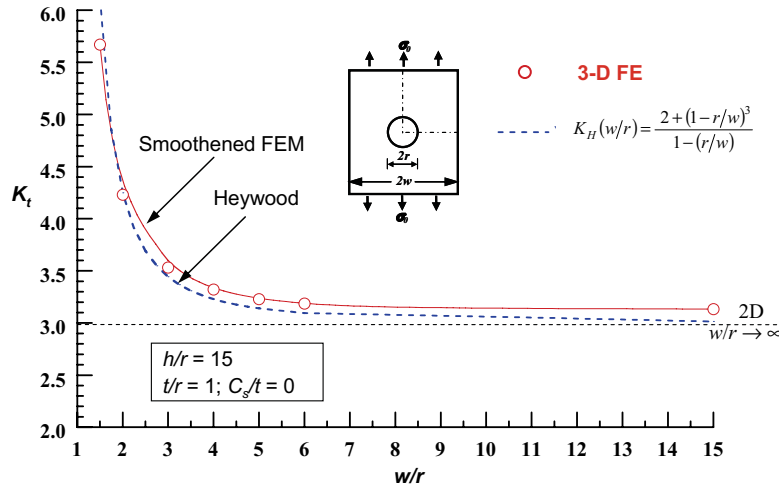
Figure 14: Effect of w/r on Stress Concentration K_t for a Straight-Shank Hole
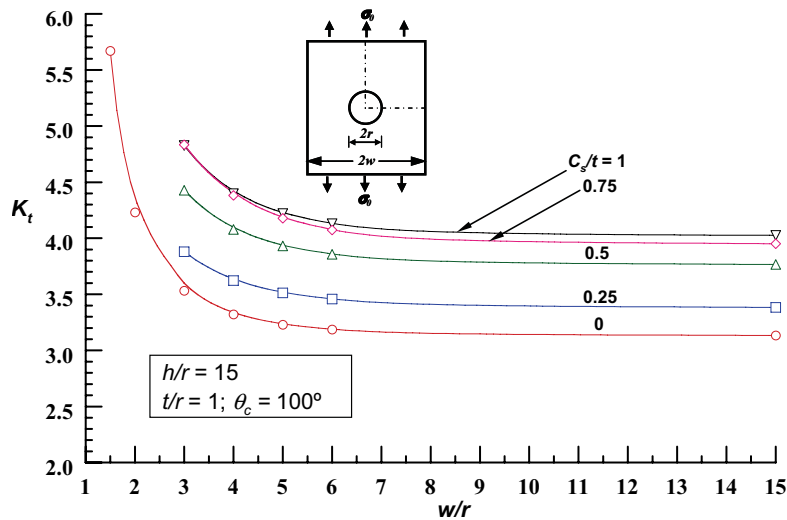
Figure 15: Effect of w/r on Stress Concentration K_t for Countersunk Holes

Table 2: Stress Concentration K_t ($w/r = h/r = 15$) from FEA

C_s/t	t/r							
	0.00	0.40	0.50	0.67	1.00	2.00	4.00	10.00
0.00	3.000	3.072	3.083	3.101	3.134	3.183	3.160	3.121
0.25	3.000	-	3.261	-	3.384	3.526	3.711	-
0.50	3.000	-	3.510	-	3.767	4.036	4.368	-
0.75	3.000	-	3.616	-	4.026	4.526	5.095	-
0.85	3.000	-	-	-	4.056	-	-	-
0.90	3.000	-	-	-	4.040	-	-	-
1.00	3.000	-	3.580	-	3.952	4.533	5.530	-

Table 3: The K_t Results for Finite Width Plates from FEA

C_s/t	w/r values						
	1.5	2	3	4	5	6	15
0.00	5.670	4.231	3.532	3.323	3.233	3.187	3.134
0.25	-	-	3.880	3.623	3.514	3.457	3.384
0.50	-	-	4.428	4.078	3.931	3.857	3.767
0.75	-	-	4.827	4.398	4.220	4.130	4.026
1.00	-	-	4.834	4.381	4.178	4.073	3.952

2. K_t is a coupled nonlinear function of (C_s/t) and t/r, and the two effects cannot be separated.

3. K_t can be approximated by a linear function of θ_c over the range of angles $60^\circ \le \theta_c \le 130^\circ$ with as the baseline data.

4. K_t increases as w/r decreases and it becomes a constant value for large w/r. The width (w/r) effect can be represented by Heywood's width correction equation for 2-D problems.

Based on these results and limiting solutions (will be stated later), a general K_t equation is developed here so that a designer can use it in their preliminary designs.

The K_t equation may be represented as a product of four functions, namely, $K_{SS}(t/r)$ for thickness effect in SS hole, K_{Cs} ((C_s/t), t/r) for countersunk effect, $K_H(w/r)$ for plate width effect, and K_{θ_c} (θ_c) to account for θ_c correction. The general

K_t equation is

$$K_t =$$
$$K_{SS}(t/r) \times K_{C_S} (C_s/t, t/r) \times K_H (w/r) \times K_{\theta_c} (\theta_c) \tag{2}$$

The finite width effect is introduced through Heywood's 2-D stress concentration equation. The 2-D SCF varies from 3 for large w/r to ∞ for $w/r = 1$. The width effect equation is

$$K_H (w/r) = \frac{2 + (1 - r/w)^3}{1 - (r/w)} \tag{3}$$

This equation was verified later by a 2-D FE analysis in Bhargava (2006). Having selected $K_H(w/r)$, the remaining three functions become a correction to 2-D SCF due to the 3-D and countersink geometry effects. The functions K_{ss}, K_{Cs} and K_{θ_c} must vary from unity to a finite value depending on the hole geometry. The limiting conditions that these three functions have to satisfy are:

a) SS hole $((C_s/t) = 0)$
$K_{Cs} = K_{\theta_c} = 1$ and $K_{SS} = 1$ for plane stress $(t/r \to 0)$ and plane strain $(t/r \to \infty)$ conditions.

b) Countersunk hole ($C_s/t \neq 0$)
  $k_{\theta_c} = 1$ if $\theta_c = 100°$ and $k_{\theta_c} \neq 1$ if $\theta_c \neq 100°$.

The K_{ss}, K_{Cs} and K_{θ_c} are determined by fitting equations to the FE results generated in the previous section. The K_{ss} is obtained from SS data, K_{Cs} from countersink data for $\theta_c = 100°$, and finally K_{θ_c} from one countersunk hole geometry with different θ_c values. The FE results used for fitting the K_{ss} and K_{Cs} equations are listed in Table 2.

7.1 The K_{ss} Equation Fit

The SS hole ($(C_s/t) = 0$) results in Table 2 are normalized by 3 (2-D SCF) and used to perform the K_{ss} equation fit. The form of the function chosen is such that it satisfies the limiting conditions that $K_{SS} = 1$ for $t/r \to 0$ (plane-stress) as well as $t/r \to \infty$ (plane strain). The equation is written in the form

$$K_{SS}(t/r) = 1 + \frac{a(t/r)^{m_1}}{b + (t/r)^{m_2}} \quad (4)$$

The four constants a, b, m_1 and m_2 are determined by the minimization of error between the equation and the FE results and the subsequent reduction of the constants to a simple form. Note that constants a, b, m_1 and m_2 are temporary variables chosen for curve fit and they do not have any meaning beyond this section. The resulting K_{ss} equation is

$$K_{SS}(t/r) = 1 + \frac{0.5(t/r)^{0.6}}{10 + (t/r)^{1.6}} \quad (5)$$

A comparison of the Eq. (5) with the FE results is shown in Fig. 16. The K_{ss} Eq. (5) agrees within 0.5% of the FE results and the correlation factor of the fit was greater than 0.98.

7.2 The $K_{Cs}(C_s/t, t/r)$ Equation Fit

The FE K_t results for the countersink hole in Table 2 are normalized by SS ($C_s/t = 0$) data and these results were used to perform a multi-parameter fit in t/r and C_s/t to obtain the K_{Cs} equation. A simple quadrating polynomial in (C_s/t) multiplied by

the t/r power function was chosen.

$$K_{Cs}\left(\frac{C_s}{t}, \frac{t}{r}\right) =$$
$$1 + a_1 \left(\frac{C_s}{t}\right)\left(\frac{t}{r}\right)^{b_1} - a_2 \left(\frac{C_s}{t}\right)^2 \left(\frac{t}{r}\right)^{b_2} \quad (6)$$

Through the multi-parameter fit, the constants a_1, a_2, b_1 and b_2 were determined. These constants were further simplified to arrive at simple values. The resulting equation is

$$K_{Cs}\left(\frac{C_s}{t}, \frac{t}{r}\right) =$$
$$1 + 0.4\left(\frac{C_s}{t}\right)\left(\frac{t}{r}\right)^{0.6} - 0.1\left(\frac{C_s}{t}\right)^2 \left(\frac{t}{r}\right)^{0.3} \quad (7)$$

Figure 17 compares the equation $K_t = 3 \times K_{SS} \times K_{Cs}$ with the FE data in Table 2 for different values of (C_s/t) and t/r. The solid lines represent the equation and the symbols represent the FE data. The maximum difference between the equation and the FE data is about 3% and the correlation factor of the equation with the FE data is greater than 0.99. Thus, the K_{Cs} equation is sufficiently accurate to account for the effect of countersunk depth and plate thickness.

7.3 The K_{θ_c} Equation Fit

As illustrated in Figs. 7 and 8, the FE results show that K_t is independent of the countersink angle θ_c for small variations ($\pm 10°$) from the baseline case of $\theta_c = 100°$. However, for large variations of θ_c, is a function of θ_c and over the range $60° \leq \theta_c \leq 130°$ it can be represented by a linear equation (see Fig. 8). Therefore, K_{θ_c} is represented by

$$K_{\theta_c}(\theta_c) = \left\{ 1 + \frac{m(\theta_c - 100°)}{K_{t@\theta_c = 100°}} \right\} \quad (8)$$

where m is the slope of K_t versus θ_c plot and $K_{t@\theta_c = 100°}$ is the SCF for $\theta_c = 100°$.

$$K_{t@\theta_c=100°} = K_{SS}(t/r) \times K_{Cs}(C_s/t, t/r) \times K_H(w/r) \quad (9)$$
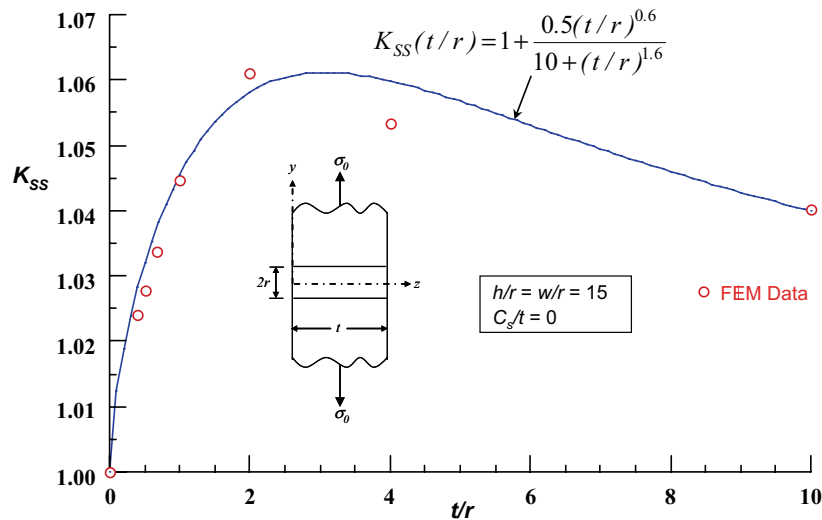
Figure 16: 3-D stress concentration factor for a straight-shank hole (wide plate)
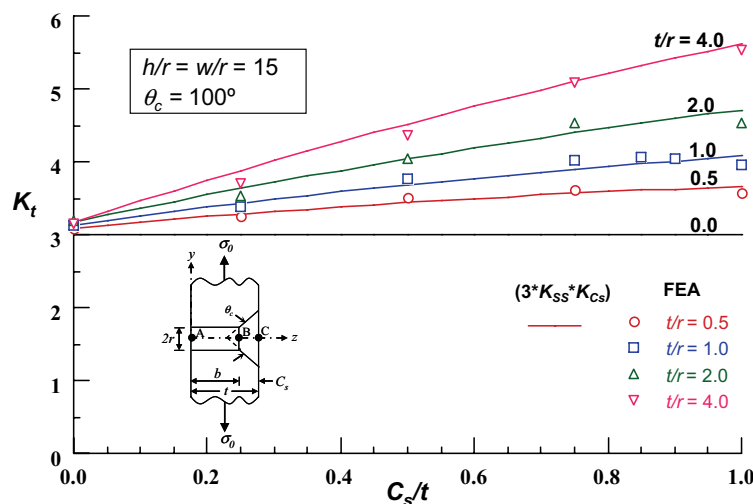
Figure 17: Comparison of 3-D SCF Equation (Thickness and Countersink Effect) with FEA Results
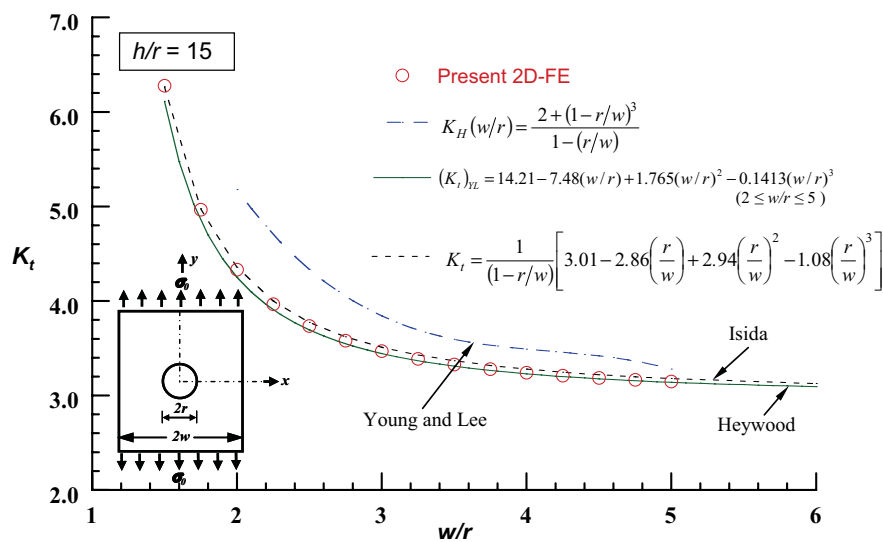
Figure 18: Comparison of 2-D SCF from Various Solutions for Finite Width Plate

Table 4: Summary of all *m* Values for Different C_s/t and t/r Values with $w/r = 15$

t/r	C_s/t				
	0.00	0.25	0.5	0.75	1.00
0.5	0.0	0.0027	0.0064	0.0093	0.0085
1.0	0.0	0.0032	0.0084	0.0141	0.0153
2.0	0.0	0.0036	0.0104	0.0175	0.0205
4.0	0.0	0.0053	0.0146	0.0258	0.0385

The slope of the line (*m*) is 0.0032 over $60° \leq \theta_c \leq 130°$ for $C_s/t = 0.25$ and $t/r = 1$. (see Fig. 8). Calculated slopes (*m*) for different (C_s/t) and t/r wide plates ($w/r = h/r = 15$) are listed in Table 4. The correlation factor of the fit was greater than 0.99. The plot of *m* versus t/r for different (C_s/t) values is shown in Fig. 12 by the use of symbols. Since *m* varies with both C_s/t and t/r, a power law equation in (t/r) was proposed in the form

$$m(C_s/t, t/r) = A_1 (t/r)^\lambda \qquad (10)$$

where A_1 and λ are functions of C_s/t. The *m* reduces to 'zero' for (C_s/t) = 0 (SS hole). Through a multi-parameter fit to (C_s/t) and (t/r), the functions for A_1 and λ were determined and they are

$$A_1 (C_s/t) = \left(\frac{C_s}{t}\right)\left[0.005 + 0.039\left(\frac{C_s}{t}\right) - 0.029\left(\frac{C_s}{t}\right)^2\right] \qquad (11)$$

$$\lambda (C_s/t) = \left(\frac{C_s}{t}\right)\left[2 - 3.3\left(\frac{C_s}{t}\right) + 2\left(\frac{C_s}{t}\right)^2\right] \qquad (12)$$

Finally the general K_t equation for the countersunk rivet hole of any (C_s/t), t/r, θ_c and w/r is given as

$$K_t = K_{SS}(t/r) \times K_{Cs}(C_s/t, t/r) \times K_H(w/r) \times K_{\theta_c}(\theta_c) \qquad (13)$$

Each of these functions are

$$K_{SS}(t/r) = 1 + \frac{0.5(t/r)^{0.6}}{10 + (t/r)^{1.6}} \qquad (14)$$

$$K_{Cs}\left(\frac{C_s}{t}, \frac{t}{r}\right) = 1 + 0.4\left(\frac{C_s}{t}\right)\left(\frac{t}{r}\right)^{0.6} - 0.1\left(\frac{C_s}{t}\right)^2\left(\frac{t}{r}\right)^{0.3} \qquad (15)$$

$$K_H(w/r) = \frac{2 + (1 - r/w)^3}{1 - (r/w)} \qquad (16)$$

and

$$K_{\theta_c}(\theta_c) = \left\{1 + \frac{m(\theta_c - 100°)}{K_{t@\theta_c=100°}}\right\} \qquad (17)$$

For special cases, the above equation simplifies to:

(a) *Countersink Angle (θ_c) is 100°*

$$K_t = K_{t@\theta_c=100°}$$
$$= K_{SS}(t/r) \times K_{Cs}(C_s/t, t/r) \times K_H(w/r) \qquad (18)$$

(b) *Wide Plate and $\theta_c = 100°$*

$$K_t = 3 \times K_{SS}(t/r) \times K_{Cs}(C_s/t, t/r) \qquad (19)$$

8 Verification of K_t Equation

8.1 Comparison with present FE Results

The K_t Eq. (2) was verified by comparing it with the FE results used for fitting the equation and by the new data generated for this purpose. The comparisons were made first for the wide plate (w/r =15) and $\theta_c = 100°$, then for the wide plate (w/r =15) for different θ_c values, and finally for finite width plates.

(a) *Wide plate ($w/r = h/r = 15$) and $\theta_c = 100°$*
   Figure 19 shows the comparison of the FE results and Eq. (2) for different (C_s/t) and t/r
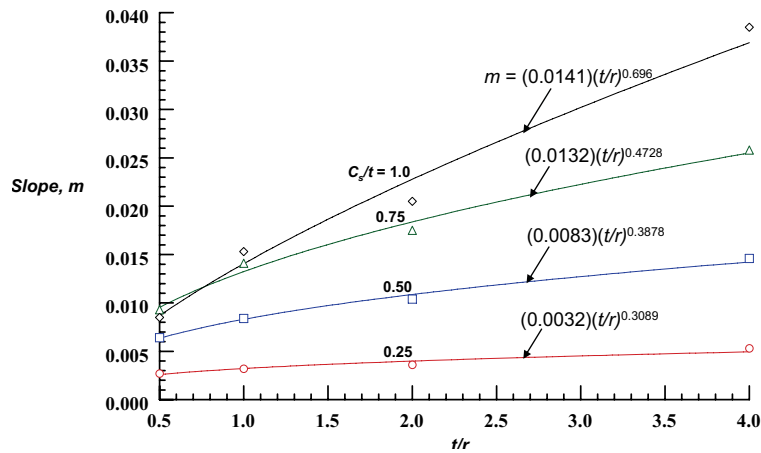
Figure 19: Variation of m with t/r for Different C_s/t Values
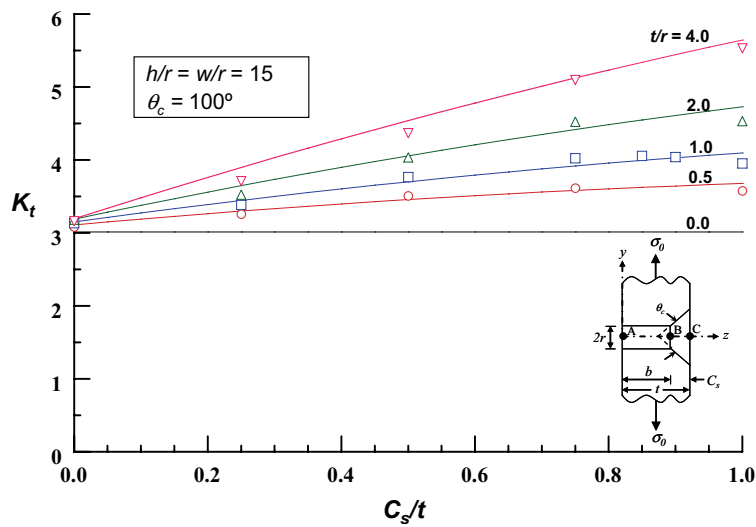
Figure 20: Comparison of Eq. (2) with FEA for Wide Plate ($w/r = h/r = 15$)
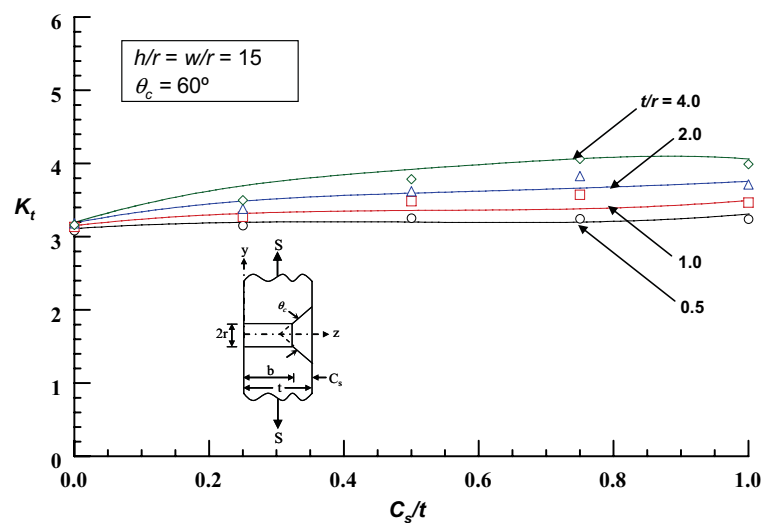
Figure 21: Comparison of Eq. (2) with FEA for $\theta_c = 60^\circ$ ($w/r = h/r = 15$)
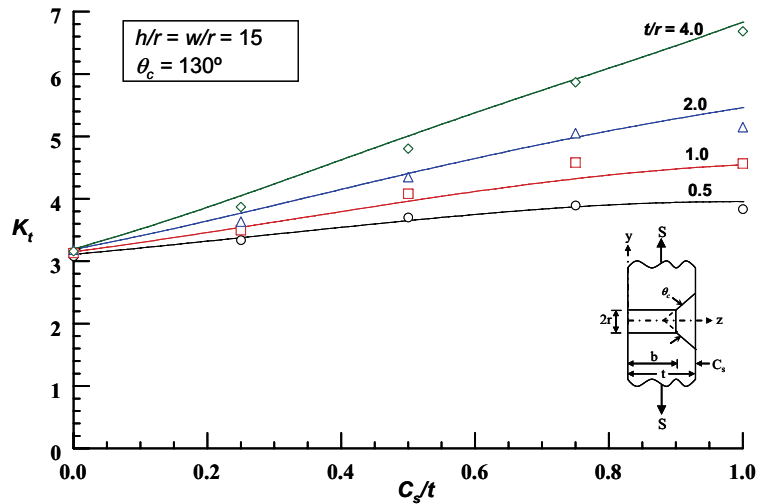
Figure 22: Comparison of Eq. (2) with FEA for $\theta_c = 130^\circ$ ($w/r = h/r = 15$)
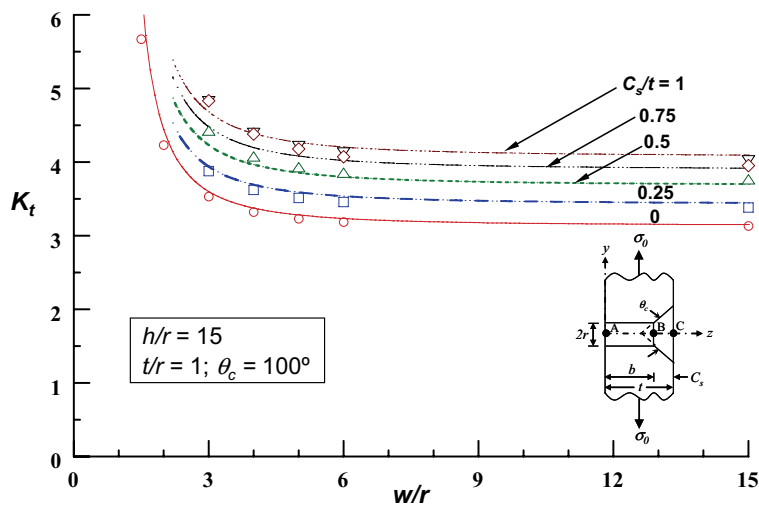
Figure 23: Comparison of Eq. (2) with FEA for Finite Width Plates ($t/r = 1$; $h/r = 15$)
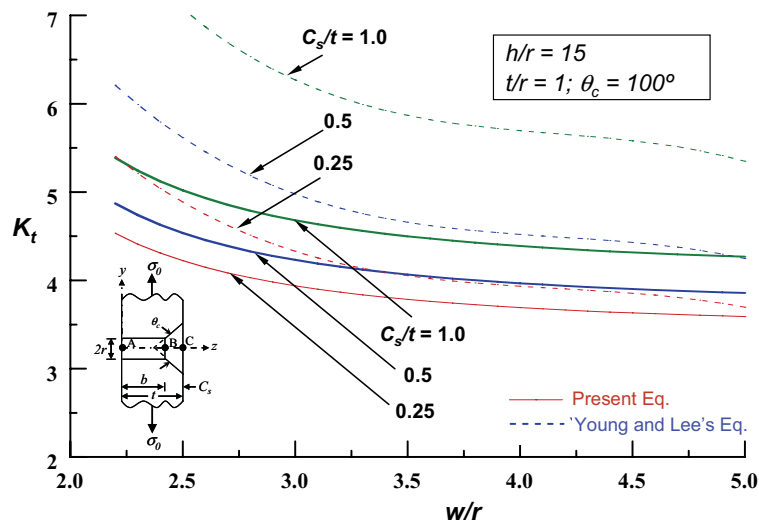
Figure 24: Comparison of Present and Young and Lee's K_t Equation Results as a Function of w/r ($t/r = 1$)

Table 5: Percent Difference Between Eq. (2) and FEA for a Wide Plate ($w/r = h/r = 15$

C_s/t	$\%Diff. = \frac{K_{t_{eq}}(\theta_c) - K_{t_{FEA}}}{K_{t_{FEA}}} \times 100$							
	t/r							
	0.00	0.40	0.50	0.67	1.00	2.00	4.00	10.00
0.00	0.5	0.9	0.9	0.8	0.5	0.2	1.1	0.4
0.25	0.5	-	1.2	-	1.8	3.5	<u>5.0</u>	-
0.50	0.5	-	-1.5	-	-1.7	0.6	4.0	-
0.75	0.5	-	-0.9	-	-2.6	-2.4	0.6	-
0.85	0.5	-	-	-	-1.5	-	-	-
0.90	0.5	-	-	-	-0.3	-	-	-
1.00	0.5	-	2.8	-	3.7	4.3	2.1	-

Table 6: Percent Difference Between Eq. (2) and FEA for Finite Width Plates ($t/r = 1$; $h/r = 15$)

C_s/t	$\%Diff. = \frac{K_{t_{eq}}(\theta_c) - K_{t_{FEA}}}{K_{t_{FEA}}} \times 100$						
	w/r						
	1.5	2	3	4	5	6	15
0.00	12.7	<u>5.0</u>	2.0	1.6	1.5	1.5	0.5
0.25	-	-	1.5	1.9	2.2	2.3	1.8
0.50	-	-	-4.4	-2.7	-1.9	-1.4	-1.7
0.75	-	-	<u>-7.2</u>	-4.5	-3.2	-2.6	-2.6
1.00	-	-	-3.2	0.2	2.2	3.3	3.7

values. The percent difference between the two results is summarized in Table 5. The maximum error in the equation is about 5% for $t/r = 4$ and $C_s/t = 0.25$, and it is less for all other cases analyzed.

(b) *Wide Plate and Different θ_c*
Figures 20 and 21 compare K_t from Eq. (2) with FE results for $\theta_c = 60°$ and $130°$ for different values of C_s/t and t/r. The percent error between the two is about 5% or less for both extreme angles.

(c) *Finite Width Plate and $\theta_c = 100°$*
Figure 22 shows a comparison between the FE results and Eq. (2) for finite width plates for different C_s/t. The percent difference between the two results is summarized in Table 6. The difference is less than or equal to 5% for all cases except for $C_s/t = 0.75$ and $w/r = 3$, where the difference is about 7%. The error is large for a very narrow width plate $w/r = 1.5$, which is not a practical case.

Based on the above comparison it is concluded that the Eq. (2) is accurate for a wide range of t/r, C_s/t, w/r and θ_c. The maximum error is about 5% or less for most of the cases, except for a few configurations where the error could be as high as 7%.

8.2 Comparison with Young and Lee's Design Equation

In 1993, Young and Lee proposed a design equation based on their FE analyses and British Aerospace's experimental design equation for the width effect. The K_t equation is represented by $K_{t_{YL}}$ and is given by

$$K_{t_{YL}} = (K_{C_S}(C_s/t))_{YL} \times (K_w(w/r))_{YL} \qquad (20)$$

where

$$(K_{C_S}(C_s/t))_{YL} = 0.959 + 0.673(C_s/t)$$

$$(K_w(w/r))_{YL} =$$
$$14.21 - 7.48(w/r) + 1.765(w/r)^2 - 0.1413(w/r)^3$$

Note that $K_{t_{YL}}$ is not a function of t/r and θ_c, and limited to $w/r \leq 5$. This equation was intended for aircraft joint configurations. The Eq. (2) and Young and Lee's Eq. (5) were compared for four plate thicknesses, namely, $t/r = 0.5, 1, 2$ and 4, for a wide range of w/r, (C_s/t) and $\theta_c = 100^o$. Only the comparison for $t/r = 1$ is presented in Figs. 38. From this comparison, it can be concluded that the two K_t equations differ widely and this difference may be as small as 'zero' or as large as 55%. Because the present K_t equation is based on an accurate FE model results and a detailed analysis, Eq. (2) is believed to be accurate.

8.3 Comparison of FE with Cheng's Experiment

Because K_t Eq. (2) was developed using configurations different from those in Cheng's experiment, therefore the equation is verified by comparing it with FE results for these configurations. Cheng's experimental configurations and the associated FE results are listed in Table 1. The difference between FE results and the K_t equation are listed in Table 7. The difference is less than 5% except for very thick plate ($t/r = 5.79$), where the difference is about 5.9%. Thus, K_t Eq. (2) is accurate and can be used for a wide range of countersunk hole configurations in a plate subjected to tensile loading.

9 Conclusions

A detailed three-dimensional finite element stress analysis was conducted on countersunk rivet hole in a plate subjected to tensile loading. The analysis included a wide range of countersunk depths ($0 \leq C_s/t \leq 1$), plate thicknesses ($0.5 \leq t/r \leq 10$), countersunk angles ($60^o \leq \theta_c \leq 130^o$) and plate widths ($1.5 \leq w/r \leq 15$). The stress concentration $K_t(z)$, along the edge formed by the intersection of $y = 0$ plane and the hole boundary was analyzed. The maximum value of the stress concentration is the stress concentration factor K_t, and its variation with hole geometries and plate width are assessed.

The FE results show that K_t is influenced by the countersunk angle θ_c, the countersunk depth ratio

(C_s/t), the thickness ratio t/r and the width ratio w/r. The K_t occurs at or near the countersink. However, for thicker plates ($t/r \geq 2$) and shallow countersink depths ($C_s/t \leq 0.25$) holes, K_t occurs slightly away from the edge (5% of t), towards the SS portion of the hole. The K_t increases monotonically with plate thickness (t/r) and C_s/t except at $C_s/t = 1$ for moderately thin plates $t/r \leq 2$. Both t/r and C_s/t have a nonlinear coupled relationship with K_t. The countersunk angle has a very small impact on K_t for small deviations ($\pm 10^o$) from $\theta_c = 100^o$. However, for large variations of θ_c, K_t increases with θ_c and this variation over the range $60^o \leq \theta_c \leq 130^o$ can be approximated by a linear equation. The K_t increases with decreasing w/r and it becomes infinite as w approaches r; whereas for $w/r > 6$, K_t is unaffected by w/r.

The present FE results also confirm the results and trends that are observed in the literature. The present FE results for the straight shank hole in wide plate agree with Sternberg and Sadowsky and Shivakumar and Newman and they also agree with revised results of Shivakumar and Newman for countersink holes. Because of coarse FE mesh used in Young and Lee, the equation grossly overestimates K_t for many cases.

Based on the FE results and the limiting conditions of configurations, a general K_t equation for SCF was developed. The equation is given by

$$K_t =$$
$$K_{SS}(t/r) \times K_{C_S}(C_s/t, t/r) \times K_H(w/r) \times K_{\theta_c}(\theta_c)$$

$$K_{SS}(t/r) = 1 + \frac{0.5(t/r)^{0.6}}{10 + (t/r)^{1.6}}$$

$$K_H(w/r) = \frac{2 + (1 - r/w)^3}{1 - (r/w)}$$

and

$$K_{\theta_c}(\theta_c) = \left\{ 1 + \frac{m(\theta_c - 100^o)}{K_{t@\theta_c=100^o}} \right\}$$

The K_t equation is accurate within 5% of the finite element data for a wide range of widths, countersunk depths, plate thicknesses and θ_c, except for a few cases where the error could be as large as 7%. Young and Lee's equations varied considerably from the present equation. The difference

Table 7: Verification of Present K_t Eq. (2) for Cheng's Experimental Models

Model#	θ_c Degrees	K_t		$\%Diff. = \frac{K_{t_{eq}}(\theta_c) - K_{t_{FEA}}}{K_{t_{FEA}}} \times 100$
		Present FEA	Eq. (2)	
1	60	3.79	4.39	4.0
2	80	4.07	4.48	4.3
3	82	4.10	4.58	5.9
4	82	4.02	4.39	4.1
5	82	4.02	4.26	1.8
6	82	4.34	4.78	2.6
7	90	4.11	4.39	4.0

may be as small as zero or as large as 55%. In summary, the stress concentration equation presented in this paper is general, accurate, and satisfies all limiting cases.

References

ANSYS 10.0, ANSYS Inc., Canonsburg, PA

Bhargava, A. (2006): Three-Dimensional Tensile Stress and Strain Concentration Equations for a Countersunk Hole. Ph.D. Dissertation, North Carolina Agricultural and Technical State University, Greensboro, NC.

Chen, Wen-Hwa; Chen, Cheng-Hung (2005): On Three-Dimensional Fracture Mechanics Analysis by an Enriched Meshless Method. *CMES: Computer Modeling in Engineering & Sciences*, vol. 8, no. 3, pp. 177-190.

Cheng, Y. F. (1978): Stress-Concentration Factors for a Countersunk Hole in a Flat Bar in Tension and Transverse Bending. *J. Appl. Mech.*, vol. 45, no. 4, pp. 929-932.

Folias, E. S.; Wang, J. J. (1990): On the Three-Dimensional Stress Field Around a Circular Hole in a Plate of Arbitrary Thickness. *Comput. Mech.*, vol. 6, no. 3, pp. 379-391.

Green, A. E. (1948): Three-Dimensional Stress Systems in Isotropic Plates. I. *Trans. Royal Soc. London*, ser. A, vol. 240, pp. 561-597.

Heywood, R. B. (1952): *Designing by Photoelasticity*. Chapman and Hall, London.

Li1, Q.; Shen, S.; Han, Z. D.; S. N. Atluri (2003): Application of Meshless Local Petrov-Galerkin (MLPG) to Problems with Singularities, and Material Discontinuities, in 3-D Elasticity. *CMES: Computer Modeling in Engineering & Sciences*, vol. 4, no. 5, pp. 571-585.

Neuber, H. (1946): *Theory of Notch Stresses: Principles for Exact Stress Calculation*. J. W. Edwards (Ann Arbor, Michigan).

Pilkey, W. D. (1997): *Peterson's Stress Concentration Factors*, 2nd Edition. John Wiley & Sons, Inc.

Savin, G. N. (Eugene Gros, transl.) (1961): *Stress Concentration Around Holes*. Pergamon Press, Inc.

Shivakumar, K. N.; Bhargava, A.; Hamoush, S. (2006): An Equation for Stress Concentration Factor in Countersunk Holes. *CMC: Computers, Materials & Continua*, vol. 3, no. 2, pp. 97-106.

Shivakumar, K. N.; Newman, J. C. Jr. (1992): Three-Dimensional Stress Concentration Factor in Straight-Shank and Countersunk Rivet Holes in Plates Subjected to Various Loading Conditions, *NASA TP 3192*.

Shivakumar, K. N.; Newman, J. C. Jr. (1995): Three-Dimensional Stress Concentration Equations for Straight-Shank and Countersunk Rivet Holes in Plates Subjected to Various Loading Conditions. *Jl. Applied Mechanics, Trans. of ASME*, vol. 62, pp. 248-249.

Sternberg, E.; Sadowsky, M. A. (1949): Three-

Dimensional Solution for the Stress Concentration Around a Circular Hole in a Plate of Arbitrary Thickness. *J. AppI. Mech.*, vol. 16, no. 1, pp. 27-38.

Whaley, R. E. (1965): Stress-Concentration Factors for Countersunk Holes. *Exp. Mech.*, vol. 5, no. 8, pp. 257-261.

Young, J. B.; Lee, K. K. (1993) Stress concentration factors in countersunk holes. *Aeronautical J*, pp. 267-276.

Zienkiewicz, C. O.; Taylor, L. R. (1989): *The Finite Element Method, Vol I: Basic formulations and linear problems*. London: McGraw-Hill.